# Social isolation uncovers a circuit underlying context-dependent territory-covering micturition

Minsuk Hyun[a,b], Julian Taranda[c], Gianna Radeljic[a,b], Lauren Miner[a,b], Wengang Wang[a,b], Nicole Ochandarena[a,b], Kee Wui Huang[a,b], Pavel Osten[c], and Bernardo L. Sabatini[a,b,1]

[a]Howard Hughes Medical Institute, Harvard Medical School, Boston, MA 02115; [b]Department of Neurobiology, Harvard Medical School, Boston, MA 02115; and [c]Cold Spring Harbor Laboratory, Cold Spring Harbor, NY 11724

The release of urine, or micturition, serves a fundamental physiological function and, in many species, is critical for social communication. In mice, the pattern of urine release is modulated by external and internal factors and transmitted to the spinal cord via the pontine micturition center (PMC). Here, we exploited a behavioral paradigm in which mice, depending on strain, social experience, and sensory context, either vigorously cover an arena with small urine spots or deposit urine in a few isolated large spots. We refer to these micturition modes as, respectively, high and low territory-covering micturition (TCM) and find that the presence of a urine stimulus robustly induces high TCM in socially isolated mice. Comparison of the brain networks activated by social isolation and by urine stimuli to those upstream of the PMC identified the lateral hypothalamic area as a potential modulator of micturition modes. Indeed, chemogenetic manipulations of the lateral hypothalamus can switch micturition behavior between high and low TCM, overriding the influence of social experience and sensory context. Our results suggest that both inhibitory and excitatory signals arising from a network upstream of the PMC are integrated to determine context- and social-experience-dependent micturition patterns.

micturition | social hierarchy | pons | hypothamaus

The control of urine output, or micturition, is necessary for the survival of animals. Mice, like many mammals, innately modulate micturition in response to internal and environmental cues and alter the spatiotemporal patterns of urine output depending on their strain, sex, and position in the social hierarchy. For example, male mice that detect competitors or potential mates (1) assiduously deposit urine throughout the environment, a process often referred to "territorial marking" or "scent marking." Social experience further modulates the extent and pattern of such urine marking by adult males. For example, "dominant" mice vigorously urinate with small and dispersed urine spots whereas "subordinate" males limit urination to large, individual spots, often located in the corners of the territory (2, 3). Therefore, urine release reflects the integration and processing of many signals and factors, including external stimuli, enteroception, and past social experience. However, unlike many other highly regulated motor outputs, micturition is carried out by the coordinated activity of only three muscles—contraction of the bladder wall detrusor muscle and relaxation of the internal and external urethral sphincters (4).

The brainstem pontine micturition center (PMC), also eponymously referred to as Barrington's nucleus, is the brain output nucleus that controls the bladder and, therefore, processes and relays information that regulates micturition (3–10). Recent studies have begun to shed light on how different cell types in the PMC work together to coordinate bladder output. Activation of glutamatergic neurons in and around the PMC quickly and robustly triggers micturition (9). Within this population, neurons marked by expression of corticotropin-releasing hormone (*Crh*, also known as corticotropin-releasing factor) bilaterally innervate the sacral spinal cord where polysynaptic pathways that innervate the bladder wall arise (3). Activation of these PMC

*Crh*-expression neurons triggers or facilitates urine output (3, 6, 7, 9). Estrogen receptor 1 (*Esr1*)-expressing glutamatergic neurons also innervate the distal cord and, when activated, relax the urinary sphincter and rapidly trigger robust urine output (7).

Interestingly, each of these neuron populations may control different aspects of micturition behavior. The sphincter is directly controlled by *Esr1*-expressing and potentially other glutamatergic neurons (9), but not by the *Crh*-expressing population (7), suggesting that activity in the former but not the latter may be necessary to initiate voluntary micturition. On the other hand, loss- and gain-of-function manipulations of PMC *Crh*-expressing neurons alter patterns of bladder contractility and urine output, suggesting that these neurons may control micturition patterns rather than individual micturition events (6, 9). Neurons in the PMC, including *Crh*-expressing and sphincter-controlling neurons, receive inputs from distributed circuits across the brain that presumably carry pro- and antimicturition information that may be further processed in the PMC before relay to the spinal cord (3, 9, 10).

To examine the pathways that modulate micturition in response to social experience and external stimuli, we adapted a behavioral paradigm to modulate micturition patterns of male mice. We found that the propensity of each mouse to cover the territory with urine—referred to here as "territory covering micturition" or TCM—depends on its strain, social experience, and olfactory context. Socially housed male C57BL/6J mice do not display robust TCM, but this behavior can be induced by social isolation. Brain-wide mapping of inputs to *Crh*-expressing PMC neurons suggested that the connectivity upstream of these neurons is largely unaffected by social isolation. In contrast, analysis of Fos protein revealed differences in activity in many

## Significance

Vertebrates control the release of urine to mediate physiological functions as well as for social communication. The release of urine, or micturition, is controlled by the brain and is influenced by many internal and external factors. In mice, these include social standing, sensory context, and past experience as well as the state of the bladder. We study the brain circuits that control micturition in mice and uncover pathways by which the patterns of urine release are altered in response to changes in social experience and olfactory stimuli.

NEUROSCIENCE

brain areas in socially isolated vs. group-housed mice and in a few areas in urine- vs. saline-exposed mice. Comparing the Fos patterns of males that exhibit high and low TCM, we identified brain areas that may carry diverse TCM-regulating signals. Chemogenetic manipulations of the lateral hypothalamus (HY), one of the modulated areas upstream of the PMC, bidirectionally alters TCM. These findings provide insights into the circuits governing micturition and motivate next steps to fully trace the neural pathway that mediates the sensorimotor transformation underlying an innate behavior.

## Results

**Social Isolation Reveals Extensive Territory-Covering Micturition.** To assess micturition behavior in male mice, we placed group-housed (GH) C57BL/6J males in cages with either a urine stimulus or a saline control (Fig. 1). In both contexts, most C57BL/6J males either did not deposit urine or did so in several large spots near the corner of the cage (Fig. 1A). This pattern of urination is associated with subordinate males and with females (2). A few male mice (6 out of 36 mice) covered the territory when exposed to urine but not when exposed to saline (GH-urine: $89 \pm 22$ marks; GH-saline: $39 \pm 16$ marks; $n = 36$ and 18 mice; $P = 0.3$ Mann–Whitney $U$ test, Fig. 1B).

We hypothesized that variability in individual experience and the changes it induces in each animal (e.g., stress and hormonal factors) may hinder the ability to induce robust TCM in urine-exposed males. To examine TCM behavior in the absence of varying social experience, we socially isolated C57BL/6J males after weaning. Once the animals reached adulthood (after postnatal day 84) (Fig. 1A), we monitored TCM as above in the presence of saline or urine. In contrast to GH animals, the majority of socially



A  C57BL/6J adult males

B  C57BL/6J adult males

C  GH-Urine / GH-Saline — SI-Urine / SI-Saline

**Fig. 1.** Social isolation reveals an innate form of context-dependent TCM. (A, Left) Housing schematics for group-housed (GH) and socially isolated (SI) mice. (Right) Representative micturition patterns revealed 1 h after GH or SI animals were placed in a test chamber with saline (blue circle) or a nonself urine (yellow circle) stimulus. (B) Number of urine marks deposited in 1 h for each experimental condition (U, urine exposed; S, saline exposed; $n = 36$ mice for GH urine, $n = 18$ mice for GH saline, $n = 25$ mice for SI urine, $n = 23$ mice for SI saline. ****$P < 0.0001$; ns, not significant; two-tailed Mann–Whitney $U$ test; not adjusted for multiple comparisons). (C) Cumulative probability distribution of distances of urine-marked pixels from the stimulus center for the four contexts with mean (solid lines) and SEM (shaded areas). **$P < 0.01$; ns, not significant; simulation by bootstrap analysis).

isolated (SI) males produced extensive TCM in the presence of urine but not saline (SI-urine: $266 \pm 21$ marks; SI-saline: $48 \pm 8$ marks; $n = 25$ and 23 mice; $P < 0.0001$ Mann–Whitney $U$ test; Fig. 1B). We observed the same patterns and urine stimulus-dependent changes in the BALB/c strain, but not in 129s and CD1 strains (*SI Appendix*, Fig. S1). Thus, social isolation reveals robust context-dependent TCM in C57BL/6J and BALB/c males.

To understand whether the spatial distribution of urine deposition is different when mice display weak or robust TCM, we calculated the cumulative distribution function (CDF) of the distances (range 0 to 15 cm) of urine marks from the center of the arena (defined as 0 cm and where the urine or saline stimulus was deposited) (Fig. 1C). Whereas GH and SI mice exposed to saline deposit urine far from the center of the cage (50% of CDF for GH-urine, GH-saline, and SI-saline was at $11.6 \pm 0.05$, $12.2 \pm 0.05$, $11.9 \pm 0.03$ cm, respectively) the SI mice exposed to urine placed urine closer to the center (50% CDF: SI-urine $9.8 \pm 0.01$ cm, $P = 0.004$ for SI-urine vs. SI-saline, $P = 0.1$ for GH-urine vs. SI-saline, test by bootstrap analysis). Thus, the micturition pattern induced by urine stimulus in SI mice arises from both an increase in the number of urine spots and increase in the amount of urine deposited near the center of the cage.
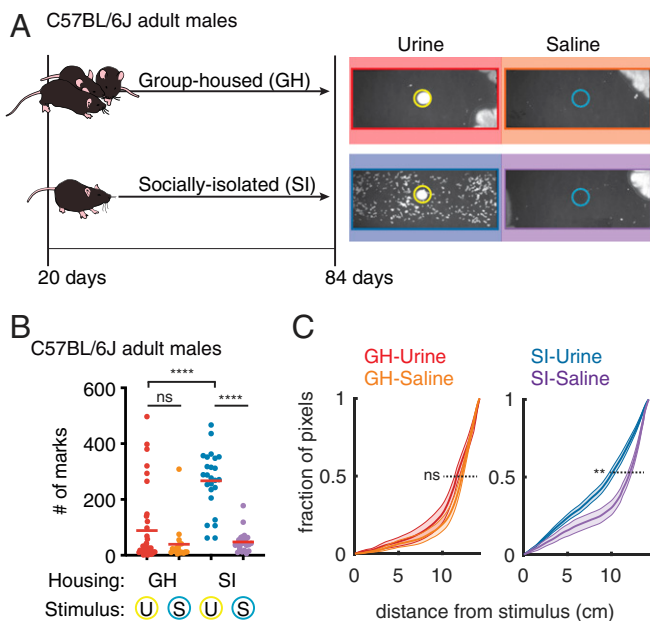
Taken together, these results demonstrate that social isolation in C57BL/6J mice reveals the capacity for robust TCM. Therefore, this behavior paradigm may be used to isolate how sensory environment modulates the bladder output in TCM, avoiding variable behavior resulting from social interactions.

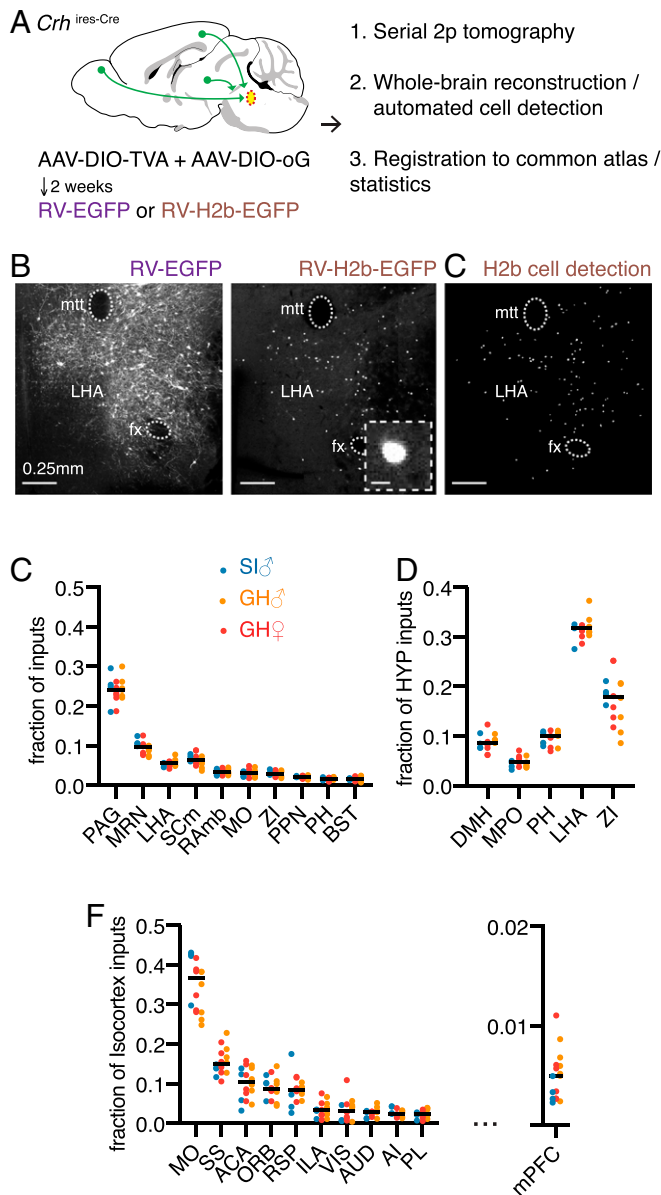**Quantitative Comparison of Brain-Wide Inputs to Crh⁺ PMC Neurons.** Approximately 50% of neurons in the PMC are glutamatergic *Crh*-expressing ($Crh^+$) neurons and activation of these cells is sufficient to induce bladder contraction and urine release in anesthetized and awake mice (3, 6, 7, 9). As social isolation can alter many aspects of brain circuitry (11) we hypothesized that the differences in TCM behavior in GH and SI males might result from changes in the projections to $Crh^+$ PMC neurons. We used whole-brain mapping of neurons labeled with retrograde transsynaptic rabies virus (RV) to quantitatively compare the distribution of cells putatively presynaptic to $Crh^+$ PMC neurons in GH and SI C57BL/6J male mice (Fig. 2A). We performed similar analysis in C57BL/6J group-housed female mice to investigate potentially sexually divergent presynaptic areas that might contribute to this male-specific behavior (12, 13).

To quantify the distributions of putative presynaptic connectivity to $Crh^+$ PMC neurons, we utilized transsynaptic rabies tracing from genetically identified cell types with automated image acquisition and analysis (14–16). RV that expresses cell-filling fluorophores, such as GFP, highlights the full neuronal morphology including axons and dendrites (Fig. 2B). Although this, in theory, can provide more information about the GFP-expressing neuron, in practice the neuropil fluorescence complicates analysis. To allow simple, automated identification of RV-labeled cell bodies, we generated a rabies virus expressing nuclear-localized GFP (RV-H2b-EGFP) (17). Tight nuclear localization of RV-H2b-EGFP facilitates precise counting of rabies-infected neurons (17), permitting an unbiased whole-brain estimate of putative inputs to $Crh^+$ PMC neurons across different housing conditions and sexes (Fig. 2C).

Cre-dependent adeno-associated viruses (AAVs) encoding avian leukosis and sarcoma virus subgroup A receptor (TVA)-mCherry and rabies glycoprotein (RVG) were injected into the PMC of $Crh^{ires\text{-}Cre}$ mice to render $Crh^+$ neurons sensitive to infection with EnvA pseudotyped RV and to complement the G-deleted RV to move transsynaptically following infection (18, 19). After 2 wk, we injected RV-H2b-EGFP into the same coordinates (Fig. 2A). As control experiments for the cell-type specificity of RV infection and transsynaptic movement, injection of EnvA pseudotyped RV without prior AAV-DIO (double-floxed

Hyun et al.
Social isolation uncovers a circuit underlying context-dependent territory-covering micturition

**Fig. 2.** Stable brain-wide connectivity of the circuitry upstream of the PMC across housing conditions and sex. (*A*) Schematic of the experimental work flow for rabies-based monosynaptic retrograde transsynaptic tracing of inputs to *Crh*$^+$ PMC neurons. Cre-dependent AAVs were injected to express TVA and optimized G glycoprotein (oG) selectively in *Crh*$^+$ PMC neurons. Following a subsequent RV injection, the brains were imaged with serial two-photon tomography, reconstructed in 3D, and registered to a reference atlas for automated analyses. (*B*) Representative coronal sections of cell-filling RV-EGFP labeled cells (*Left*) and nuclear localized RV-H2b-EGFP labeled cell (*Right Inset*) with enlarged image of one RV-labeled cell. (Scale bar, 10 μm.) in the LHA (mtt, mammillothalamic tract; fx, fornix). These images are stitched from multiple fields of view (see *Materials and Methods*). (*C*) Output of the cell-detection algorithm from the same RV-H2b-EGFP hypothalamic section as in *B*. Each dot represents a detected cell. (*D*) Top 10 putative input regions to *Crh*$^+$ PMC neurons, presented as the distribution of labeled neurons in GH-male, SI-male, and GH-females (*n* = 6 mice for GH-male, *n* = 4 mice for SI-male, *n* = 6 mice for GH-female). Differences among the groups were not statistically significant (*P* > 0.05 for all regions, Wilcoxon signed rank test, adjusted for multiple comparisons with the Benjamini, Kreiger, and Yekutieli false discovery rate approach [FDR = 0.05]). (PAG, periaqueductal gray; MRN, midbrain reticular nucleus; LHA, lateral hypothalamic area; SCm, superior colliculus, motor related; RAmb, midbrain raphé nuclei; MO, somatomotor areas; ZI, zona incerta; PPN, pedunculo-pontine nucleus; PH, posterior hypothalamic nucleus; BST, bed nuclei of the

Hyun et al.
Social isolation uncovers a circuit underlying context-dependent territory-covering micturition

inverse orientation)-TVA injection showed no rabies infection, whereas omitting AAV-DIO-RG resulted in robust starter cell labeling but no transsynaptic labeling of putative inputs (*SI Appendix*, Fig. S2 *A* and *B*).

The distribution of H2b-EGFP-labeled neurons in the three-dimensional (3D) brain volume was subsequently imaged through serial two-photon tomography (14), reconstructed, and aligned to the Allen Brain Atlas (ABA). The fraction of total RV-H2b-EGFP cells was calculated in each ABA-defined region to quantify the distribution of RV$^+$-labeled inputs (*SI Appendix*, Table S2). In the three groups (*n* = 6 GH males, *n* = 4 SI males, *n* = 6 GH females), the largest fraction of input cells originated in the periaqueductal gray (Fig. 2*D*; peri-aqueductal gray [PAG], 24.2 ± 0.6% of total inputs), followed by midbrain reticular nucleus (MRN, 9.8 ± 0.6% of total inputs).

We utilized the quantitative whole-brain rabies mapping dataset to identify components of the micturition network. Querying the Allen Brain Atlas Injection Map, we observed, consistent with previous analyses (20), that *Crh*$^+$ PMC neurons send projections to the ventrolateral part of PAG where putative inputs to *Crh*$^+$ PMC reside (*SI Appendix*, Fig. S2*C*).

Hypothalamic inputs accounted for 18% of total forebrain inputs to *Crh*$^+$ PMC neurons (*SI Appendix*, Fig. S2*D*), with the lateral hypothalamus area (LHA) and zona incerta (ZI) providing ~50% of these (Fig. 2*E*; LHA: 31.5 ± 0.5% and ZI: 17.4 ± 1.1% of hypothalamic inputs). By comparison, the medial pre-optic (MPO) area, a hypothalamic nucleus that modulates micturition (3), accounted for ~0.8% of total forebrain inputs and ~5% of hypothalamic inputs.

Other areas identified as putatively presynaptic to PMC *Crh*$^+$ neurons were the motor cortex (MO), which conveys top-down urination initiation signals to the PMC (10), and the medial prefrontal cortex (mPFC, infralimbic area + prelimbic area [ILA+PL]), a region involved in the regulation of social dominance (21, 22). MO had the highest number of RV-labeled neurons in regions of isocortex (3.1 ± 0.2% of total RV$^+$ cells, sixth overall). Within isocortex, MO was the largest source of putative PMC input, providing 35%, while the mPFC provided considerably less (Fig. 2*G*; <1% of total inputs; 5.5 ± 0.5% of isocortex inputs) (*SI Appendix*, Table S2). Additionally, extensive labeling of non-*Crh* neurons was observed within the PMC, which, considering the no-TVA and no-RVG controls described above, suggests the existence of intra-PMC connectivity (*SI Appendix*, Fig. S2*E*).

Subsets of identified putative inputs were tested for functional connectivity through in vitro electrophysiology. We injected Cre-independent ChR2 into candidate upstream regions of *Crh*$^{ires-Cre}$;*Rosa26*$^{lsl-tdTomato}$ animals in which *Crh*-expressing neurons are marked by tdTomato red fluorescence. Using whole-cell voltage-clamp recordings, we analyzed light-evoked postsynaptic currents in *Crh*$^+$ PMC neurons (23). We observed a clear monosynaptic glutamatergic current from mPFC (<1% of inputs), highlighting the sensitivity of the RV-based transsynaptic tracing (*SI Appendix*, Fig. S2 *F–I*; 35/60 *Crh*$^+$ neurons were connected). Previous functional (3, 9, 10) and anatomical analyses (8) have demonstrated input to PMC *Crh*$^+$ neurons from many of the RV-labeled brain areas, including MO, MPO, LHA,

stria terminalis. (*E*) The distribution of labeled cells across the top five hypothalamic subregions shown as the fraction of all labeled cells within the hypothalamus. (DMH, dorsomedial nucleus of the hypothalamus; PH, posterior hypothalamic nucleus). (*F*) The distribution of labeled cells across the top 10 cortical subregions (*Left*) and medial prefrontal cortex (*Right*) shown as fraction of all labeled cells within the isocortex. (MO, somatomotor areas; SS, somatosensory areas; ACA, anterior cingulate area; ORB, orbital area; RSP, retrosplenial area; ILA, infralimbic area; VIS, visual areas; AUD, auditory areas; AI, agranular insular area; PL, prelimbic area).

and PAG, supporting the specificity of the transsynaptic labeling by RV.

To test the hypothesis that circuit wiring differences contribute to the differences in TCM behavior, we compared the distribution of putative inputs to PMC $Crh^+$ neurons in GH males, SI males, and GH females. The brain-wide distributions of $RV^+$ neurons were similar across all three conditions ($P > 0.05$, Wilcoxon signed rank test, adjusted for multiple comparisons with the Benjamini, Kreiger, and Yekutieli false discovery rate approach (FDR = 0.05); Fig. 2 $D$–$F$), suggesting that, despite the behavioral divergence, GH and SI males as well as GH females largely share a similar structural network upstream of the PMC.

**Identification of Upstream Networks That Are Differentially Regulated in Each Micturition Mode.** Although retrograde transsynaptic rabies has been proposed to depend on both anatomy (i.e., the existence of a synapse) and functional properties (i.e., the strength of the synapse) (24), there are likely changes in synaptic properties of neurons that project to the PMC that are not revealed by the distribution of RV labeling. In addition, changes in the intrinsic properties of PMC neurons could be induced by housing conditions. Nevertheless, current-clamp recordings revealed only a moderate increase in the number of action potentials evoked by current injections in SI males (*SI Appendix*, Fig. S3 *B* and *C*), suggesting small changes in intrinsic excitability of these cells. However, the frequencies of both spontaneous inhibitory postsynaptic currents (sIPSCs) and spontaneous excitatory postsynaptic currents (sEPSCs) are higher in SI males, especially the sIPSCs (*SI Appendix*, Fig. S3*E*). This is consistent with enhanced probability of release from inhibitory inputs to $Crh^+$ neurons or increased spontaneous activity of local inhibitory neurons in the PMC brain slice, and, together with the rabies tracing data, suggest functional changes upstream of the PMC in SI animals without large-scale rewiring.

To identify brain regions with potentially differential activity that might contribute to the modulation of micturition behavior, we examined whole-brain patterns of Fos protein expression following different experiences. As we had identified two features that regulate the degree of TCM—social experience and exposure to urine—we examined each of these separately.

First, group-housed and socially isolated C57BL/6J males were exposed to urine in a behavioral arena as in Fig. 1 for 1 h. In this experiment, both sets of animals were exposed to the same sensory environment and only the previous social experience of mouse differed. One hour after the end of urine exposure, the animals were killed and perfused and the brains cleared using iDisco+ (25). Subsequently, endogenous Fos protein was immunolabeled and visualized using fluorophore-conjugated secondary antibody. Both far-red (Fos) and green (autofluorescence) fluorescence were detected via light-sheet imaging, followed by automated image-based identification of Fos protein-expressing cells and registration through the ClearMap pipeline (Fig. 3 *A* and *B*; full dataset in *SI Appendix*, Table S3).

SI animals showed higher brain-wide $Fos^+$ cell counts (Fig. 3 *C* and *D*; GH gray: 329,846 ± 7,393; SI gray: 465,235 ± 14,750, $P < 0.0001$; Mann–Whitney $U$ test). Notably, the greater $Fos^+$ count in socially isolated animals was due to increases in the isocortex (Fig. 3*D*; GH-isocortex: 73,041 ± 4,649; SI-isocortex: 193,785 ± 8,839, $P < 0.0001$; Mann–Whitney $U$ test). Almost all subregions of the isocortex (Fig. 3*E*) had significantly increased numbers of cells expressing Fos, with the exception of a subset of motor cortex associated with licking behaviors (anterolateral motor cortex, Fig. 3*C*) (26). In contrast, "subcortical" regions (pons, midbrain, thalamus in the ABA) had decreased numbers of $Fos^+$ cells in SI mice compared to in GH mice (Fig. 3 *D*–*F*, *SI Appendix*, Fig. S5; GH-subcortex: 100,854 ± 3,739; SI-subcortex: 66,172 ± 1,592, $P < 0.00001$; Mann–Whitney $U$ test). Thus, our data suggest that changes in activity across the brain, as opposed to in a single brain region, underlie the differences in behaviors of socially isolated and group-housed mice.

Second, we compared the whole-brain Fos expression patterns of SI males exposed to urine vs. saline (Fig. 4*A*; $n = 4$ mice each, *SI Appendix*, Fig. S6*A*). As expected, SI males exposed to urine marked the territory more robustly than SI males exposed to saline (*SI Appendix*, Fig. S6*B*). The distributions of endogenous Fos protein induced by these different contexts were compared using region of interest (ROI)- and voxel-based statistical tests, corrected for multiple comparisons with a false discovery rate of 0.05. Voxel-based analysis revealed significant activation in the PMC of the urine-exposed mice, confirming previous findings (3) (Fig. 4*B*). We also observed correlated changes in Fos expression in related structures, suggesting experience-specific activity patterns (*SI Appendix*, Fig. S6*C*).

Region-based analysis showed fewer Fos-expressing cells in the hypothalamus in animals exposed to urine (Fig. 4*C*; HY; q < 0.001, FDR = 0.05). Many areas in the hypothalamus were differentially regulated, including regions previously implicated in socially motivated behaviors such as lateral preoptic (LPO) and MPO areas (Fig. 4*D* and *SI Appendix*, Fig. S7). LHA, a major hypothalamic input to the PMC (Fig. 2*E*), had significantly fewer Fos-labeled cells in urine-exposed groups (q < $10^{-11}$). No differences were observed in ventromedial hypothalamus (VMH) (*SI Appendix*, Table S4), an area previously implicated in male aggression (27). Outside the hypothalamus, midbrain motor regions, including subregions of the superior colliculus motor (SCm) and PAG, were selectively activated in urine-exposed groups. Voxel-based analysis yielded nearly identical results, with spatial patterns restricted to specific subhypothalamic nuclei (Fig. 4*E*).

To identify networks presynaptic to the PMC that are potentially capable of modulating TCM directly, we computationally combined the rabies-tracing anatomical data with the Fos iDisco immunostaining data. A side-by-side comparison of Fos voxel maps and the distribution of rabies-transduced cells revealed a striking spatial overlap (Fig. 4 *E* and *F*). To obtain whole-brain comparison of structure and function of the presynaptic micturition network, we generated voxelated maps of rabies inputs on the same coronal atlas based on ABA (*SI Appendix*, Fig. S7). Notably, Fos activation was seen in a region that borders anterior hypothalamic nucleus (AHN)/bed nuclei of stria terminalis (BST) that is not well defined by the ABA; however, once referenced to the spatial input map labeled by rabies, the spatial pattern match is clear (anterior posterior = −0.2 mm in Fig. 4*E* and slice 111 in *SI Appendix*, Fig. S7). This region likely corresponds to one identified in Valentino et al. (8) (their figure 4H).

To investigate coordinated network changes, we applied principal component analysis (PCA) on the $Fos^+$ cell counts in urine and saline groups (28, 29). The coordinates of each mouse in the principal component space defined by the first two principal components (PCs) revealed that the urine- and saline-exposed groups segregated along PC1 (Fig. 4*G*). Examining the PC loadings across all brain areas allowed us to visualize the brain-wide Fos expression pattern that separates the two groups (Fig. 4*H*). In general, the first PC was generated by negative weightings of cell counts in hypothalamus and positive ones in thalamus and midbrain. This indicates that the main differences between urine- and saline-exposed mice are explained by increase in Fos labeling in thalamus and midbrain and decreases in hypothalamus.

**Identification of Networks Upstream of the PMC Underlying Context-Dependent TCM.** Our data indicated that the LHA is a major hypothalamic input to the PMC and that Fos levels in this structure are low in mice that show robust TCM. In situ hybridization revealed that the rabies-labeled neurons in the LHA largely but not uniformly express genes encoding for glutamate decarboxylases (including both *Gad1* and *Gad2*, 66%, $n = 337$ cells from three mice, Fig. 5 *A*–*C*), suggesting that the LHA
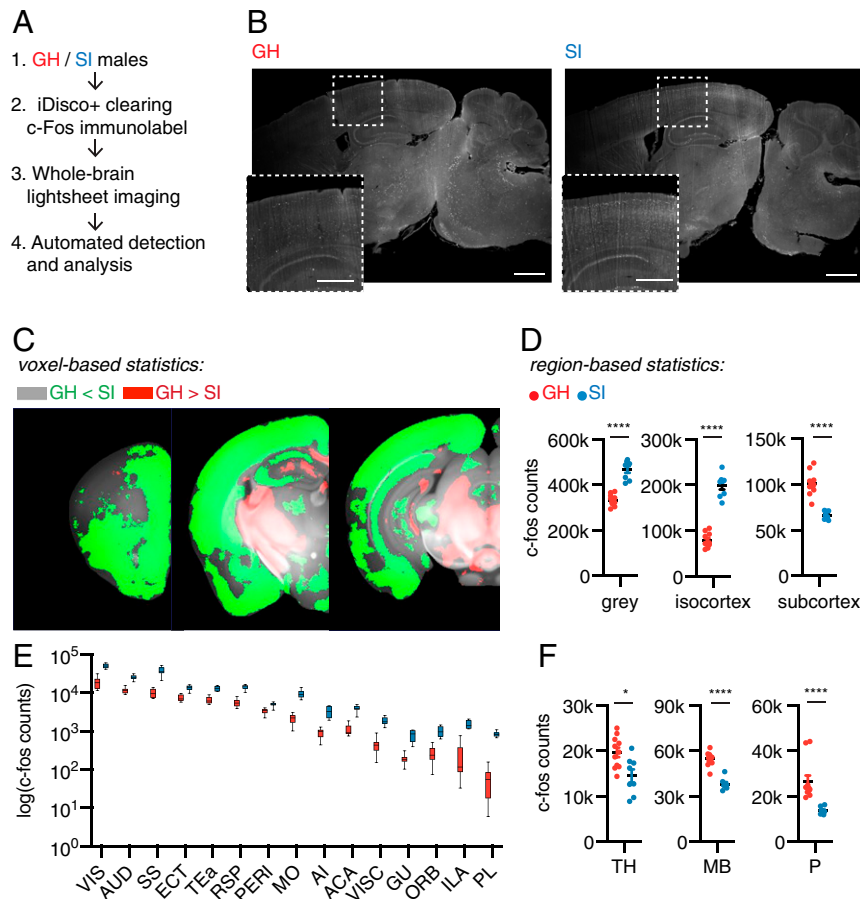
**Fig. 3.** Social Isolation induces brain-wide activity changes. (*A*) Schematic for the whole-brain Fos mapping experimental workflow: brains from GH and SI males were cleared, immmunolabeled for Fos, imaged, and analyzed. (*B*) Representative virtual sagittal section of Fos-immunolabeled brains of group-housed and singly-housed animals. The *Insets* show enlargements of the cortical regions in the dotted boxes. (Scale bar, 1 mm; 0.5 m in the *Inset*.) (*C*) Maps of voxel-based statistics analyses overlaid on the Allen Brain Reference Atlas. Green indicates statistically significant (n = 11 GH group, n = 8 SI group; q < 0.05 with FDR = 0.05) voxels with higher Fos counts in SI animals, and red indicates higher Fos counts in GH animals. (*D*) Quantification of Fos cell counts of GH and SI males in gray matter, isocortex, and subcortex (n = 11 GH group, n = 8 SI group; Mann–Whitney *U* test; ****P < 0.0001). (*E*) Quantification of Fos cell counts of GH and SI males throughout isocortex presented on a log scale, sorted by Fos counts. (VIS, visual areas; AUD, auditory areas; SS, somatosensory areas; ECT, ectorhinal area; TEA, temporal association areas; RSP, retrosplenial area; PERI, perirhinal area; MO, somatomotor areas; AI, agranular insular area; ACA, anterior cingulate area; VISC, visceral area; GU, gustatory areas; ORB, orbital area; ILA, infralimbic area; PL, prelimbic area). (*F*) Quantification of Fos cell counts of GH and SI groups in thalamus (TH), midbrain (MB), and pons (P) (Mann–Whitney *U* test, *P < 0.05, ****P < 0.001).

sends mixed GABAergic and glutamatergic input to *Crh⁺* PMC neurons. These results are consistent with previous identification of both glutamatergic and GABAergic LHA neurons projecting generally to the PMC (9). Based on these findings, we hypothesized that activity in the LHA may modulate the urine-induced switch in micturition behavior in SI males. If the LHA primarily inhibits the PMC (as suggested by the predominance of rabies-labeled GABAergic neurons) and TCM (as suggested by higher LHA Fos levels in low TCM contexts), then 1) suppression of the LHA should elicit TCM in a saline-exposed SI mice, and 2) activation LHA should inhibit TCM in a urine-exposed SI mice.

Previous studies have shown that increasing activity of *Crh⁺*, *Esr1⁺*, motor-cortex targeted, or nonspecific glutamatergic neurons in the PMC has promicturition effects, causing either urine release in awake or anesthetized animals, increasing bladder pressure, or dilating the sphincter (3, 6, 7, 9, 10). Similarly, increasing activity of glutamatergic inputs to the PMC promotes micturition (9, 10) whereas withdrawal of input and ablation or silencing of PMC glutamatergic neurons has converse effects (7, 9, 10). Therefore, activating glutamatergic or GABAergic inputs to the PMC and finding, respectively, pro- and antimicturition effects

would be a fully expected result that is firmly established in the literature. Therefore, such experiments were not repeated here.

Instead, in order to test whether the LHA is part of the circuit that determines micturition modes, we generally manipulated LHA activity, including both glutamatergic and GABAergic neurons, and examined the effects on TCM. We used the chemogenetic tools hM4Di and hM3Dq (30, 31), which are, respectively, engineered $G_{(q}$- and $G_{(i}$-coupled receptors that are activated by clozapine derived from peripherally administered clozapine-N-oxide (CNO) to either increase or reduce the activity of receptor-expressing neurons (AAV-hM4Di-mCherry or AAV-hM3Dq-mCherry, Fig. 5*D*). Activating hM4Di may also decrease the probability of action potential-evoked neurotransmitter release from expressing neurons (32). Each chemogenetic actuator or mCherry control virus was expressed in the LHA using Cre-independent AAVs and the effects of saline vs. CNO were compared on alternate days in both cohorts of mice. This study design controlled for nonspecific effects of CNO (comparison of CNO effects in designer receptor exclusively activated by designer drugs [DREADD]- vs. mCherry-expressing mice) as well as of hM4Di and hM3Dq expression (comparisons of effects of saline vs. CNO in DREADD-expressing mice and of
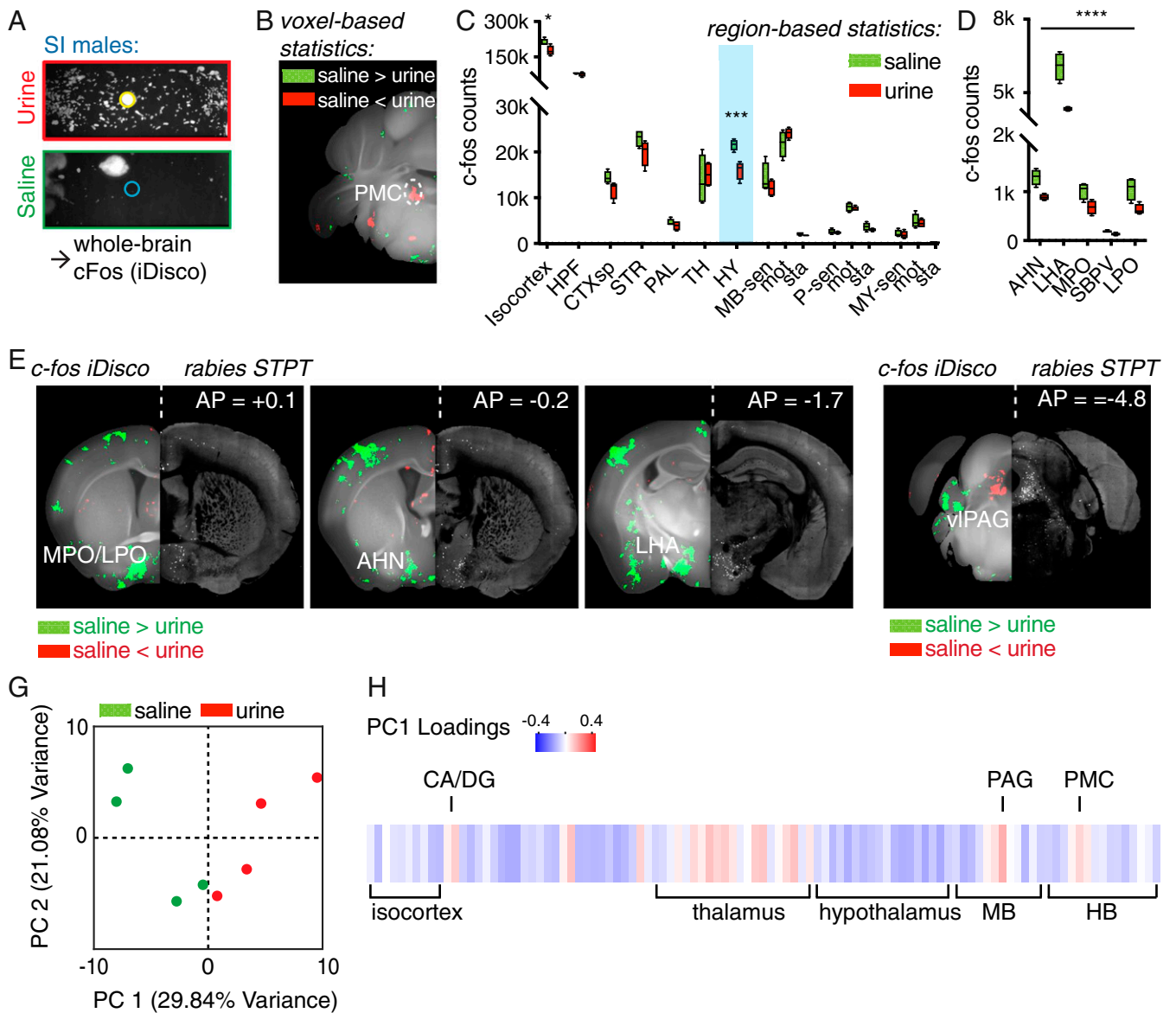
**Fig. 4.** Brain circuits upstream of PMC are differentially activated during different micturition behaviors. (*A*) Schematic of the whole-brain Fos analysis workflow: SI males were exposed to either urine or saline, which resulted in divergent TCM. One hour after the behavior, animals were perfused, the brains were cleared, immunolabeled for Fos, imaged, and analyzed (*n* = 4 each for the urine and the saline conditions). (*B*) Maps of voxel-based statistics reveal increased numbers of Fos⁺ neurons in the PMC in urine-exposed animals. Green indicate statistically significant (q < 0.05, FDR = 0.05) voxels with higher Fos counts in animals exposed to saline, and red indicates higher Fos counts in animals exposed to urine. (*C*) Fos induction in multiple brain regions from saline- and urine-exposed animals (*q < 0.05, ***q < 0.0001, FDR = 0.05). (HPF, hippocampal formation; CTXsp, cortical subplate; STR, striatum; PAL, pallidum; HY, hypothalamus; MB-sen, midbrain, sensory related; MB, midbrain, P, pons; MY, medulla; -sen, sensory related; -mot, motor related; -sta, behavioral-state related). (*D*) The five hypothalamic regions with the largest differences in Fos induction across saline- and urine-exposed animals, sorted by q values (all regions q < 0.0005; refer to *SI Appendix,* Tables S2 and S3 for full statistics). (AHN, anterior hypothalamic nucleus; LHA, lateral hypothalamic area; MPO, medial preoptic area; SBPV, subparaventricular zone; LPO, lateral preoptic area). (*E*) Hypothalamic regions with differential Fos induction that project to the PMC: voxel-based statistics map from Fos (*Left*) and corresponding RV STPT images (*Right*) of putative inputs to *Crh⁺* PMC in the same coronal slice. Each panel shows a stitched image with the left- and right-hand sides coming from different imaging modalities. (*F*) Ventrolateral segment of PAG (vlPAG), the major input to the PMC, displays differential Fos activation. (*G*) Individual mice projected onto the first two PC spaces of whole-brain Fos⁺ cell densities. (*H*) Brain-wide Fos patterns in response to urine, represented as the loadings of individual brain regions in PC1. (HB, hindbrain; CA, Ammon's horn; DG, dentate gyrus).

saline in DREADD- vs. mCherry-expressing mice). We did not examine potential changes in stress, endocrine function, locomotion, or other behaviors and aspects of physiology beyond micturition.

To test the prediction that inactivation of the LHA would elicit TCM in a saline-exposure context, we placed SI male mice in clean cages lined with filter paper and a saline stimulus. As no urine stimulus was present, control SI mice were expected to

deposit few urine marks in this condition (Fig. 1 *A* and *B*). Thirty minutes before the behavioral analysis, the animals were intraperitoneally (IP) injected with either CNO (5 mg/kg) or vehicle (Fig. 5*E*). Mice expressing hM4Di in lateral hypothalamus displayed increased TCM following CNO injection compared to after saline injection (Fig. 5 *G* and *H*; *n* = 5 hM4Di mice, hM4Di vehicle: 56 ± 33 marks, hM4Di CNO: 173 ± 16 marks, *P* = 0.043; Mann–Whitney *U* test). mCherry-expressing control animals
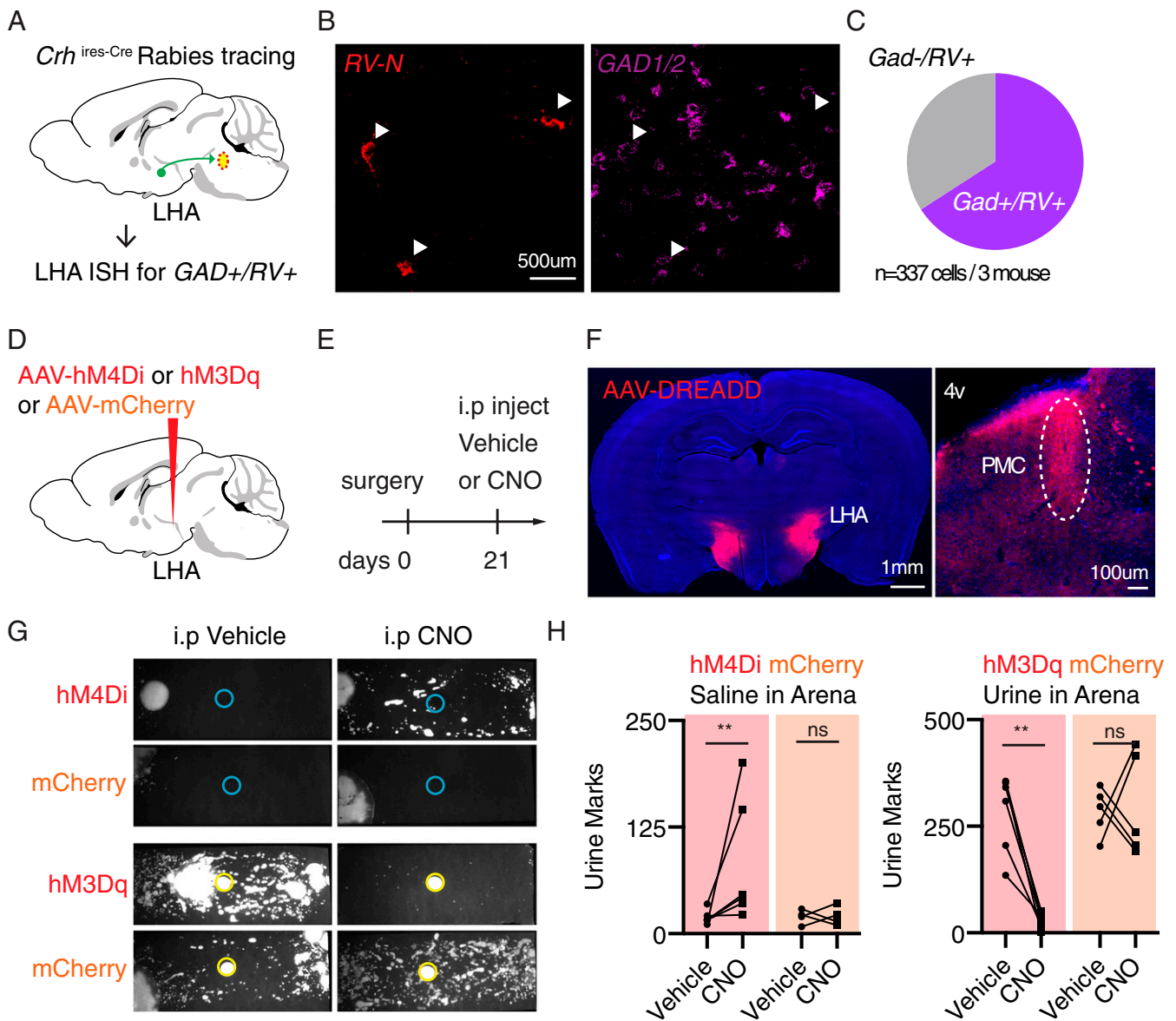
**Fig. 5.** Modal switching of micturition patterns via chemogenetic manipulation of the lateral hypothalamic area. (*A*) Experimental design to interrogate neurotransmitter content of *Crh*[+] PMC-projecting LHA neurons. Cell-type specific rabies tracing (described in detail in Fig. 2) was performed, sections including LHA were cryosectioned, and cells were classified as GAD[+] (*Gad 1* and *Gad 2*)/RV (Rabies virus nucleoprotein)[+] or GAD-/RV[+] through in situ hybridization (ISH). (*B*) Representative ISH image containing LHA. Arrowheads indicate *RV-N*^{+} cells in the *RV-N*[+] (*Left*) and *GAD1/2* (*Right*) fluorescent ISH channels. (*C*) In situ hybridization of GAD and RV in LHA reveals that a majority of cells in LHA retrogradely labeled from *Crh*[+] PMC started cells express GABA synthetic enzymes (*n* = 3 mouse, 337 LHA cells). (*D* and *E*) Experimental design. (*D*) AAVs encoding inhibitory DREADD hM4Di or excitatory DREADD hM3Dq were bilaterally injected in the lateral hypothalamic area. (*E*) Three weeks after surgery, hM4Di mice were introduced to a test cage with no urine stimulus, and hM3Dq mice were introduced to a test cage with no saline stimulus. Mice were IP injected with either vehicle or CNO 25 min before the behavior. (*F*, *Left*) Representative expression pattern of DREADD targeted toward lateral hypothalamus. (*Right*) Representative image showing DREADD-expressing fibers in the pons. The PMC is identified (oval) relative to the fourth ventricle (4v). (*G*) Example micturition patterns for mice transduced with hM4Di (*Top*) or hM3Daq (*Bottom*) DREADD or mCherry control and injected with vehicle (*Left*) or 5 mg/kg CNO (*Right*). (*H*, *Left*) More urine marks were deposited in CNO trials compared to in vehicle trials in hM4Di-transduced animals (*n* = 6 hM4Di animals, *n* = 4 mCherry controls, two-tailed Mann–Whitney *U* test, **P < 0.01, ns, not significant) exposed to saline. (*Right*) Fewer urine marks deposited in CNO trials compared to in vehicle trials in hM3Dq-transduced animals (*n* = 6 hM3Dq animals, *n* = 5 mCherry controls, two-tailed Mann–Whitney *U* test, **P < 0.01, ns, not significant) exposed to urine.

showed similar TCM on CNO- and saline-injection days ($n = 4$ mCherry mice; mCherry vehicle: 26 ± 4 marks, mCherry CNO: 12 ± 2 marks, $P = 0.93$; Mann–Whitney $U$ test).

To test the second prediction that activation of the LHA should inhibit TCM in a urine-exposure context, we placed a separate cohort of animals in clean cages lined with filter paper with urine stimulus. In this condition, control SI mice are expected to robustly cover the arena with urine (Fig. 1 *A* and *B*). Thirty minutes

before the behavioral analysis, the animals were IP injected with either CNO (5 mg/kg) or vehicle. mCherry-expressing control animals displayed robust TCM on both saline- and CNO-injected days (Fig. 5 *G* and *H*; $n = 5$ mCherry mice; mCherry vehicle: 231 ± 28 marks, mCherry CNO: 429 ± 13 marks, $P = 0.86$; Mann–Whitney $U$ test). In contrast, mice expressing hM3Dq in the LHA decreased TCM in CNO-injected days, despite the urine stimuli (Fig. 5 *G* and *H*; $n = 6$ hM3Dq mice; hM3Dq vehicle:

Hyun et al.
Social isolation uncovers a circuit underlying context-dependent territory-covering micturition

PNAS | 7 of 11
https://doi.org/10.1073/pnas.2018078118

259 ± 54 marks, hM3Dq CNO: 37 ± 7 marks, $P$ = 0.002; Mann–Whitney $U$ test).

Unfortunately, the pandemic shut down limited the number of mice that could be tested experimentally such that a replication cohort could not analyzed. Therefore, we compared the data on hand using bootstrap and receiver operator characteristics (ROC) analysis (*Materials and Methods*). The distributions of urine mark numbers for CNO- vs. vehicle-treated DREADD-expressing mice and those of CNO-treated DREADD-expressing mice vs. "all control" mice are distinct with either no or minimal overlap in their 95% confidence intervals group (*SI Appendix*, Fig. S8). This translates into near maximal area under the curve (AUC ~1, indicating near perfect discriminability) when comparing the effects of CNO in DREADD-expressing mice to control mice by ROC. Furthermore, the data from vehicle-treated hM4D- or hM3D-expressing mice are statistically indistinguishable from those from the full control group (*SI Appendix*, Fig. S8). These analyses (which treat each data point as independent and thus reduce statistical power by ignoring the paired nature of data acquisition), show that the differences between datasets are significant and not dependent on outlier data points, and that the distributions can be readily distinguished by an independent observer. Thus, these results show that activation of LHA can prevent the robust micturition behavior induced in socially isolated males by urine, whereas its suppression can mimic this behavior in socially isolated males in the absence of urine stimulus.

## Discussion

Animals select specific motor actions based on sensory information about their current environment, memories of past experiences, and internal states. Most nonreflex behaviors that are influenced by these factors are complex. This complicates directly linking neural activity to specific muscle action and obfuscates the flow and transformation of information from sensory organs to motor effectors. Studying the neural circuits underlying micturition is attractive for understanding action selection because: 1) the behavior is simple (the bladder has two modes—retention and voiding); 2) the selected action is easily observed (urine release is readily tracked in behaving and anesthetized mice); 3) the motor action is expressed with only three muscles whose activities are coordinated; and 4) the behavior is controlled by a sole effector nucleus, the PMC, onto which pathways that carry relevant information must converge.

**Social-Experience-Dependent Micturition in the Laboratory.** Rodent social-experience-dependent changes in micturition were first studied in outbred wild strains (2). Many follow-up studies have examined micturition in a variety of inbred/outbred strains (3, 6, 7, 9, 10, 33–36). Our results suggest that differences in strains and housing conditions likely contribute to variable results across studies. Group-housed males live in a complex social structure—individual mice continuously interact with cage mates, competing for resources (water/chow) and establishing a tiered social hierarchy. Each social interaction is capable of inducing transcriptional (37), electrophysiological (22, 38), and neuroendocrine (39–42) changes in the brain. Social experience and standing in these social structures affects TCM (2, 3).

We hypothesize that the lack of robust TCM in group-housed C57BL6 mice is due to the complexities of continuous social interaction. Therefore, social isolation may provide a path to bypass the challenges of experimentally monitoring and controlling social dominance. Here we exploited social isolation to restrict analysis to neural circuits that contribute to the sensorimotor transformation (i.e., urine stimulus to urine output) underlying TCM. Analysis of socially isolated mice may be similarly useful to identify pathways by which enteroceptive signals such as the filling state of the bladder converge on and are processed by the PMC.

**Combined Structure–Function Elucidation of TCM-Controlling Brain Centers.** The combined analysis of circuit architecture with trans-synaptic labeling and of behavior-specific brain activation identified functionally relevant networks controlling micturition. Structural analysis alone failed to find circuit differences that can explain varying behavior as the distribution of putative presynaptic inputs to $Crh^+$ PMC neurons in GH males, SI males, and females—groups with divergent TCM—differed only minimally. Previously, a nearly identical approach uncovered connectivity differences of hypothalamic circuitry in males and females (43) and across subregions of small thalamic nuclei (17), suggesting that we were not limited by the method of analyses. Although we cannot account for unknown differences that are beyond the resolution of our methods—such as induction of synaptic plasticity or morphological changes—it is evident that the three groups share largely comparable structural connectivity of the upstream PMC micturition network.

Instead, we discovered changes in activity patterns, as reported by Fos protein levels, between TCM conditions in many brain areas. These findings are consistent with studies in head-restrained mice that revealed distributed representations of behavioral variables (44–46) that are gated by behavioral states (47). In contrast, comparisons of the whole-brain Fos induction patterns between different sensory and behavioral contexts within an environmental condition (e.g., urine- vs. saline-exposed SI males) revealed relatively few affected brain areas. Combined with analysis of brain-wide rabies-tracing data, our work identified brain areas that potentially carry significant task-specific information to guide context- and state-dependent TCM via the PMC. Chemogenetic manipulation of one of these areas, the LHA, confirmed its contribution to determining micturition modes in SI male mice. Future work will examine the contribution of the LHA and its subcircuits to micturition control in GH male and female mice.

The large-scale changes resulting from chronic social isolation are consistent with the brain-wide up-regulation of $Tac2$ induced by acute social isolation in adult mice (11). Our data and this previous study illustrate the need to investigate circuits throughout the brain rather than focusing on individual candidate areas. New technologies to record single-neuronal-level activity throughout the large brain volumes (48, 49) together with extensive connectivity atlases (e.g., Allen Brain Connectivity Mapping) will shed light on how coordinated activity dynamics control context-dependent TCM.

**The PMC as Integrating Multiple Micturition-Controlling Signals.** Our findings support the hypothesis that the PMC functions as an integration center of pro- and antimicturition signals that arrive from different sources, including the LHA. Our and published data suggest that the projection from the LHC to the PMC has complex effects, beyond simply promoting and inhibiting, on micturition. Verstegen et al. (9) described that LHA inputs to the PMC are a mixture of glutamatergic and GABAergic and demonstrated that selective activation of glutamatergic inputs stimulates micturition. We confirmed the mixed nature of the LHA to PMC inputs but found that the majority express inhibitory markers. Furthermore, the results of combined chemogenetic modulation of glutamatergic and GABAergic LHA populations suggest that, in SI animals, the LHA provides a net inhibitory input to the PMC that suppresses micturition. We propose that the relative activation of inhibitory and excitatory inputs from the LHA to the PMC dynamically regulates micturition modes expressed in different behavioral states.

Our study did not determine if the activity of the direct projection from the LHA to the PMC is responsible for the behavioral effects shown in Fig. 5*H*. However, the only known outputs from the brain to the bladder-control circuits in the spinal cord are via the PMC, and previous studies (3, 6, 7, 9, 50) have shown that increasing the activity of $Esr1^+$, $Crh^+$, motor-cortex targeted, or

nonspecific glutamatergic PMC neurons increases bladder pressure, relaxes the sphincter, or induces micturition. Therefore, it is reasonable to infer that increasing excitation to these promicturition neurons is also promicturition. We speculate that a brain area that projects directly to the PMC, whose activity is modulated in different micturition contexts, and that has been shown by chemogenetics and optogenetics to affect micturition does so via its projections to the PMC. However, manipulations of the LHA may have additional circuits as well as indirect effects due potential changes in nonmicturition aspects of physiology that also contribute to the perturbation of micturition.

We previously reported that silencing of the MPO area, one of the upstream micturition networks of the PMC, masks social-rank-dependent TCM (3). Future studies are needed to understand how activity in the LHA is coordinated with that of the MPO area and other micturition-regulating structures, such as motor cortex and PAG. As PAG receives ascending sacral afferent inputs (4, 51) as well as projections from hypothalamus and dorsal pons (20), a ventrolateral PAG–PMC loop may be a key circuit controlling voluntary micturition.

Interestingly, the spatial patterns of TCM induced by the MPO area and LHA manipulations are quite different: inhibition of the LHA led mice to extensively cover the territory with small urine spots whereas inhibition of MPO caused mice to produce large circular urine spots (3). This is consistent with the proposal that the different elements of the network presynaptic to the PMC encode different information and differentially impact patterns of activity in the PMC. This hypothesis is further supported by findings that motor cortex input to the PMC is critically involved in "micturition initiation" (10).

**PMC as a Switch.** The activity of motor cortex input to the PMC increases its activity only during the initiation of each micturition bout, whereas the PMC sustains increased activity throughout the micturition event (50). This suggests that PMC internal dynamics and connectivity may contribute to a switch between voiding and retention modes. Indeed, manipulations of $Crh^+$ PMC neurons indicate that these are not simple promicturition cells but instead regulate the frequency and duration of micturition events or bladder contractions (6, 7, 9). These results are consistent with a potential role of $Crh^+$ neurons in modulating TCM modes which are characterized by stimulus-induced changes in the frequency and pattern of urine output.

Intranuclear connectivity of the PMC, whose existence is suggested by the rabies-tracing studies presented here, may contribute to integrating and linking different inputs to the control of micturition and micturition patterns. For example, recurrent connectivity between the glutamatergic cell types that modulate the sphincter and the bladder may coordinate prolonged contraction of the bladder wall and rapid relaxation of the urinary sphincter, whereas activity of local interneurons may modulate the switch between different micturition modes seen in different contexts. Elucidating these potential function of intra-PMC and PMC-to-PMC transhemispheric projections requires further studies.

## Materials and Methods

Further information and requests for reagents may be directed to Bernardo Sabatini (bsabatini@hms.harvard.edu).

**Mice.** We used the following mouse lines in the study: wild-type C57BL/6J (The Jackson Laboratory 000664); wild-type BALB/c (The Jackson Laboratory 000651); wild-type 129s (The Jackson Laboratory 002448); wild-type CD1 (Charles River 022); knockin mice with an internal ribosome entry site (ires)-linked Cre recombinase gene downstream of the $Crh$ locus ($Crh^{ires-Cre}$, The Jackson Laboratory 012704) (52, 53); and Cre-dependent tdTomato ($ROSA^{lsl-tdTomato}$, The Jackson Laboratory 007914) reporter mice (52). All mice used in this study were between 2 and 5 mo of age. Animals were kept on a 12:12 light/dark cycle or a reversed cycle under standard housing conditions. All behavioral experiments were conducted during the dark cycle. All experimental manipulations were

performed in accordance with protocols approved by the Harvard Standing Committee on Animal Care, following guidelines described in the NIH *Guide for the Care and Use of Laboratory Animals* (54). All mice brain coordinates in this study are given with respect to Bregma; anterior–posterior (A/P), medial–lateral (M/L), and dorsal–ventral (D/V).

**Virus Preparation.** Recombinant AAVs of serotype 1, 5, and 9 encoding a downstream gene under the control of a CMV–chicken β–actin (CBA), Ef1a, or hSyn promoter was used throughout the study. Details of the viruses including specific promoters and serotypes are mentioned individually in *Materials and Methods*. All of the AAVs were used at the concentration of $10^{12}$ genome copies/mL and purchased from commercial vector cores (University of North Carolina, University of Pennsylvania, and AddGene). EnvA pseudotyped rabies viruses (RV-EGFP, RV-H2b-EGFP) were generated in-house as previously described (17, 55).

**Stereotaxic Intracranial Injections and Fiber Optic Implantation.** All surgery was performed in aseptic conditions. Mice were anesthetized with 2 to 3% isoflurane and placed in a stereotactic frame (David Kopf Instruments). Skulls were exposed and small holes were drilled into the skull. Viruses were injected (100 to 200 nL total volume) at a rate of 100 nL min$^{-1}$ via glass pipettes with tip size of ~40 μm. Mice were given pre- and postoperative oral carprofen (MediGel CPF, 5 mg/kg/day) as an analgesic, and monitored daily for at least 4 d postsurgery. All coordinates that were used in this study were relative to Bregma (in millimeters) and were as follows: for mPFC: 2.1 A/P, 0.35 M/L, 2.0 D/V; for LHA: −1.5 A/P, 1.1 M/L, 5.2 D/V; for PMC: −5.3 A/P, 0.68 M/L, 3.5 D/V.

**Social Isolation.** Postnatal day (p) 15 to 20 (p15 to 20) wild-type mice of four different strains were purchased from The Jackson Laboratory and Charles River. At postnatal day 21, the mice were separated from the mothers and housed in groups of two to three (pair housed or group housed), or in singles (singly housed). The mice were housed in fully ventilated cages, and the handling was minimized. Individual cages were changed every 2 wk.

**TCM Behavior.** Adult (older than 70 d old) male mice were separated into individual fresh cages lined with filter paper (28 × 11 cm, Whatman 05-714-5) with an olfactory stimulus (50 μL male urine or saline, randomly assigned) added to the center. Male urine was freshly collected and pooled from urine of 16 to 20 group-housed BALB/c males (for C57BL6/J, 129s, and CD1 behavior) or C57BL/6J males (for BALB/c males). After 1 h in the arena, mice were removed, the distribution of urine spots on the paper was examined with fluorescence imaging as previously described (3). To quantify spatial distribution of urine marks throughout the cage, the urine mark image was thresholded and converted into a mask, which was used to calculate the distance distribution of all urine-covered pixels to the stimulus center. Statistical significance was judged by simulation—for each housing condition (GH or SI) all of the spatial CDF was put into one list and randomly assigned to two groups. P value was calculated by how often one observed the differences out of 1,000 reruns. All behavior experiments were done in at least two replicates.

**Whole-Brain Rabies Tracing.** TVA, a receptor of an avian virus envelope protein (EnvA), and RG were introduced specifically in $Crh^+$ PMC neurons through two AAVs encoding Cre-dependent genes (AAV9-CBA-DIO-TVA-mCherry and AAV9-CBA-DIO-optimized G) injected unilaterally (100 nL of 1:1 mixture). After 2 wk of expression, 200 nL of RG-deleted (ΔRG) rabies virus pseudotyped with EnvA (RV-EGFP or RV-H2b-EGFP) was injected intracranially. RV-injected animals were perfused transcardially with ice-cold phosphate-buffered saline (PBS) followed by 4% PFA, 7 d after RV injection. After a 24-h postfix in 4% PFA, brains were kept in 0.7% glycine solution for 48 h. The brain was stored in PBS before embedding in 4% agarose in 0.05 M phosphate buffer (PB), cross-linked in 0.2% sodium borohydride solution, and imaged with a high-speed multiphoton microscope with integrated vibratome sectioning (x-y resolution of 1 μm; z-step of 50 μm; TissueCyte 1000, TissueVision) as described before (14). The raw image files were corrected for illumination, stitched two-dimensionally (2D), and aligned in 3D. EGFP-positive neurons automatically detected by a convolutional network trained to recognize cytoplasmic neuronal cell body labeling (56) were visually validated, reconstructed in 3D, and their spatial information was registered by affine followed by B-spline transformation using the software Elastix (57) to a 3D reference brain based on the Allen Brain Atlas (58, 59). The number of total input neurons in the brain was normalized by the total number of RV-positive neurons. Parts of pons (P), hindbrain (H), and main olfactory bulb (MOB) were damaged or missing

Hyun et al.
Social isolation uncovers a circuit underlying context-dependent territory-covering micturition

PNAS | 9 of 11
https://doi.org/10.1073/pnas.2018078118

NEUROSCIENCE

during the dissection and excluded from the analysis. Rabies experiments were done in three replicates. Samples with mechanical damage or mis-targeted virus were excluded.

**Electrophysiology.** Acute slice electrophysiology experiments were done as previously described (60, 61). The 300-μm slices were cut in ice-cold solution containing (in millimoles) 25 NaHCO3, 25 glucose, 1.25 NaH$_2$PO$_4$, 7 MgCl2, 2.5 KCl, 0.5 CaCl2, 11.6 ascorbic acid, 3.1 pyruvic acid, and 110 choline chloride. Slices were transferred for 10 min to a holding chamber containing choline-based solution consisting of (in millimoles): 110 choline chloride, 25 NaHCO3, 2.5 KCl, 7 MgCl2, 0.5 CaCl2, 1.25 NaH$_2$PO$_4$, 25 glucose, 11.6 ascorbic acid, and 3.1 pyruvic acid before transferring to a second room temperature chamber with artificial cerebrospinal fluid (ACSF) for at least 30 min. Recordings were performed at 32 °C in carbogen-bubbled ACSF using Cs-based internals for voltage-clamp measurements [in millimoles: 135 CsMeSO$_3$, 10 Hepes, 1 ethylene glycol-bis(β-aminoethyl ether)-N,N,N',N'-tetraacetic acid (EGTA), 3.3 QX-314 (Cl$^-$ salt), 4 Mg-adenosine triphosphate (ATP), 0.3 Na-guanosine triphosphate (GTP), 8 Na$_2$-phosphocreatine, pH 7.3 adjusted with CsOH; 295 mOsm·kg$^{-1}$] and K-based internals for current-clamp measurements (in millimoles: 135 KMeSO$_3$, 3 KCl, 10 Hepes, 1 EGTA, 0.1 CaCl$_2$, 4 Mg-ATP, 0.3 Na-GTP, 8 Na$_2$-phosphocreatine, pH 7.3 adjusted with KOH; 295 mOsm·kg$^{-1}$). For optogenetics experiments, a 100-nL mixture of AAV5-Ef1a-DIO-ChR2 and AAV1-hSyn-Cre was coinjected in the mPFC. Five-millisecond duration light pulses from a 473-nm laser 5 to 10 mW/mm$^2$ measured at the sample plane were used.

**Electrophysiology Analysis.** All analysis regarding electrophysiological properties were performed using custom-written MATLAB script. In short, action potentials were identified from peaks crossing 0 mV. Action potential threshold was determined from the voltage at the time corresponding to the peak of the second derivative of the voltage and maximum rate of change of the voltage (dV/dT) was measured from the peak of the first derivative. For ChR2-evoked EPSC analysis, resting membrane potential was measured as the median of potentials during periods of the sweep that had no current injection, and the peak postsynaptic current was measured manually. For spontaneous EPSC/IPSC analysis, candidate EPSC/IPSC amplitude was identified by the findpeaks function in MATLAB and manually verified by an experimenter.

**Whole-Brain Fos Staining and Imaging.** Single-housed adult C57BL/6J males and pair-housed adult C57BL/6J males (older than 70 d old) were separated into individual fresh cages lined with filter paper (28 × 11 cm, Whatman 05-714-5) with an olfactory stimulus (50 μL male urine or saline, randomly assigned) added to the center. After 1 h in the arena, mice were returned to the home cage. One hour later, the mice were deeply anesthetized with isoflurane and transcardially perfused with ice-cold saline followed by 4% PFA. After 24-h postfix in 4% PFA, brains were kept in 0.05 M PB solution.

Within 3 wk of perfusion, the left hemispheres of the brain samples were cut and immunolabeled for Fos and subsequently cleared using iDisco+ protocol (Certerra) (25). In short, the samples were pretreated with methanol, permeabilized with solution containing dimethyl sulfoxide, blocked in donkey serum, and passively immunolabeled for Fos (9F6 rabbit mAb 2200, Cell Signaling Technology) and Alexa Fluorophore conjugated 647 secondary antibodies. Then, the samples were cleared with a combination of methanol and dichloromethane as previously described (25). Experiments were done in two replicates, and samples with mechanical damage were excluded.

**Whole-Brain Fos Analysis.** Cleared samples were imaged in sagittal orientation (right lateral side up) on a light-sheet fluorescence microscope (Ultramicroscope II, LaVision Biotec) equipped with a sCMOS camera (Andor Neo) and a 4×/0.5 objective lens (MVPLAPO 4×) equipped with a 6-mm working distance dipping cap. The samples were scanned with a step size of 3 μm using the continuous light-sheet scanning method with the included contrast blending algorithm for the 640-nm and 595-nm channels (20 acquisitions per plane), and without horizontal scanning for the 480-nm channel.

The activated Fos$^+$ neurons were automatically computationally identified and visualized in 3D. The datasets were warped in 3D by affine and B-spline transformation to an average reference mouse brain generated from 40 8-wk-old C57BL/6 brains, as described previously (19, 62).

Statistical comparisons between different groups are run based on both ROIs and evenly spaced voxels. Voxels are overlapping 3D spheres with 100-μm diameter each and spaced 20 μm apart from each other. The cell counts at a given location, Y, are assumed to follow a negative binomial distribution whose mean is linearly related to one or more experimental conditions, X: $E[Y]=\alpha+\beta X$. For example, when testing an experimental group vs. a control group, the X is a single column showing the categorical classification of mouse sample to group identification, i.e., 0 for the control group and 1 for the experimental group (63, 64). We found the maximum likelihood coefficients α and β through iterative reweighted least squares, obtaining estimates for sample SDs in the process, from which we obtained the significance of the β-coefficient. A significant β means the group status is related to the cell count intensity at the specified location. The $P$ values give us the probability of obtaining a β-coefficient as extreme as the one observed by chance, assuming this null hypothesis is true. To account for multiple comparisons across all voxel/ROI locations, we thresholded the $P$ values and reported false discovery rates with the Benjamini–Hochberg procedure (FDR = 0.05).

**In Situ Hybridization.** For fluorescent in situ hybridization, animals were anesthetized with isoflurane before decapitation, and the brains were rapidly removed and frozen. A total of 20 μm PMC coronal sections of freezing media embedded brains (Tissue-Tek O.C.T.) were prepared on cryostat (Leica, CM1950), and mounted on SuperFrost Plus glass slides (VWR) at 60-μm intervals. Multiplexed fluorescent in situ hybridization was performed using the ACDBio RNAScope reagents and protocols as previously described (3). Single-plane images of the PMC were acquired via confocal microscope (Leica SP8).

**Chemogenetic Manipulation.** hM3Dq (excitatory DREADD) or hM4Di (inhibitory DREADD) were non-Cre dependently introduced in bilateral LHA and nearby regions (AAV5-Ef1a-DO-hM3Dq, or AAV9-Ef1a-DIO-hM4Di mixed with AAV1-hSyn-Cre, 150 nL per side) of BALB/c wild-type single-housed mice. For the control mice, AAV encoding mCherry was injected instead (AAV5-hSyn-mCherry). All behavioral experiments were conducted between 3 and 5 wk postinjection. All mice were habituated for IP injections for 2 d. Then the mice were subjected to behavioral testing: 30 min before the behavior, the mice was injected IP with CNO (5 mg/kg) or volume-matched saline in the home cage. Then the mice were transferred to individual cages with either male urine (hM3Dq) or saline (hM4Di) in the center of the paper for 1 h. Behavioral experiments were done in two replicates. The filter paper was imaged and analyzed as described above.

For statistical analysis of these data, we performed boot strapping by creating 10,000 distributions generated by sampling with replacement from the data obtained from hM4D ($n = 6$ mice) or hM3D ($n = 6$ mice), or all of the control data pooled from vehicle-and CNO-treated mice expressing mCherry in the LHA. We compared the overlap and the 95% confidence intervals of the boot strapped distributions. We also performed ROC analysis by plotting true positive rate (TPR) vs. false positive rate (FPR) parametrized by a hypothetical threshold of number of urine spots that separates data from CNO-treated animals from the associated control dataset.

After behavioral experiments, animals were perfused transcardially with ice-cold PBS followed by 4% PFA. After an overnight fix in 4% PFA, brains were equilibrated in 30% sucrose for at least 48 h. Brain samples were then sliced in 50 μm using a frozen microtome (Leica) and every other section was mounted on Superfrost Plus (Fisher Scientific) slides. Slides were coverslipped with Prolong Antifade mounting media containing DAPI (Molecular Probes) and imaged with an Olympus VS120 slide-scanning microscope using a 10× objective. Injection sites were manually confirmed based on the DREADD-mCherry expression.

**Quantification and Statistical Analysis.** Data points are stated and plotted as mean values ± SEM. $P$ values are represented by symbols using the following code: * for $0.01 < P < 0.05$, ** for $0.001 < P < 0.01$, *** for $0.0001 < P < 0.001$, and **** for $P < 0.0001$. Exact $P$ values and statistical tests are stated in the figure legends. No a priori power analyses were done.

**Data Availability.** All study data are included in the article and supporting information. The code used to generate the distributions, perform ROC, and plot results for *SI Appendix*, Fig. S8 are available in Github at https://github.com/bernardosabatini/Hyun_et_al_2020.

1. J. L. Hurst, R. J. Beynon, Scent wars: The chemobiology of competitive signalling in mice. *BioEssays* **26**, 1288–1298 (2004).
2. C. Desjardins, J. A. Maruniak, F. H. Bronson, Social rank in house mice: Differentiation revealed by ultraviolet visualization of urinary marking patterns. *Science* **182**, 939–941 (1973).
3. X. H. Hou et al., Central control circuit for context-dependent micturition. *Cell* **167**, 73–86.e12 (2016).
4. W. C. de Groat, C. Wickens, Organization of the neural switching circuitry underlying reflex micturition. *Acta Physiol. (Oxf.)* **207**, 66–84 (2013).
5. M. J. Drake et al., Neural control of the lower urinary and gastrointestinal tracts: Supraspinal CNS mechanisms. *Neurourol. Urodyn.* **29**, 119–127 (2010).
6. H. Ito et al., Probabilistic, spinally-gated control of bladder pressure and autonomous micturition by Barrington's nucleus CRH neurons. *eLife* **9**, e56605 (2020).
7. J. A. Keller et al., Voluntary urination control by brainstem neurons that relax the urethral sphincter. *Nat. Neurosci.* **21**, 1229–1238 (2018).
8. R. J. Valentino et al., Evidence for widespread afferents to Barrington's nucleus, a brainstem region rich in corticotropin-releasing hormone neurons. *Neuroscience* **62**, 125–143 (1994).
9. A. M. J. Verstegen et al., Non-crh glutamatergic neurons in Barrington's nucleus control micturition via glutamatergic afferents from the midbrain and hypothalamus. *Curr. Biol.* **29**, 2775–2789.e7 (2019).
10. J. Yao et al., A corticopontine circuit for initiation of urination. *Nat. Neurosci.* **21**, 1541–1550 (2018).
11. M. Zelikowsky et al., The neuropeptide Tac2 controls a distributed brain state induced by chronic social isolation stress. *Cell* **173**, 1265–1279.e19 (2018).
12. T. Kimura, Y. Hagiwara, Regulation of urine marking in male and female mice: Effects of sex steroids. *Horm. Behav.* **19**, 64–70 (1985).
13. F. Rosell, L. R. Thomsen, Sexual dimorphism in territorial scent marking by adult Eurasian beavers (Castor fiber). *J. Chem. Ecol.* **32**, 1301–1315 (2006).
14. T. Ragan et al., Serial two-photon tomography for automated ex vivo mouse brain imaging. *Nat. Methods* **9**, 255–258 (2012).
15. I. R. Wickersham, S. Finke, K.-K. Conzelmann, E. M. Callaway, Retrograde neuronal tracing with a deletion-mutant rabies virus. *Nat Methods* **4**, nmeth999 (2006).
16. I. R. Wickersham et al., Monosynaptic restriction of transsynaptic tracing from single, genetically targeted neurons. *Neuron* **53**, 639–647 (2007).
17. G. Mandelbaum et al., Distinct cortical-thalamic-striatal circuits through the parafascicular nucleus. *Neuron* **102**, 636–652.e7 (2019).
18. E. J. Kim, M. W. Jacobs, T. Ito-Cole, E. M. Callaway, Improved monosynaptic neural circuit tracing using engineered rabies virus glycoproteins. *Cell Rep.* **15**, 692–699 (2016).
19. N. R. Wall, I. R. Wickersham, A. Cetin, M. De La Parra, E. M. Callaway, Monosynaptic circuit tracing in vivo through Cre-dependent targeting and complementation of modified rabies virus. *Proc. Natl. Acad. Sci. U.S.A.* **107**, 21848–21853 (2010).
20. R. J. Valentino, L. A. Pavcovich, H. Hirata, Evidence for corticotropin-releasing hormone projections from Barrington's nucleus to the periaqueductal gray and dorsal motor nucleus of the vagus in the rat. *J. Comp. Neurol.* **363**, 402–422 (1995).
21. F. Wang et al., Bidirectional control of social hierarchy by synaptic efficacy in medial prefrontal cortex. *Science* **334**, 693–697 (2011).
22. T. Zhou et al., History of winning remodels thalamo-PFC circuit to reinforce social dominance. *Science* **357**, 162–168 (2017).
23. L. Petreanu, D. Huber, A. Sobczyk, K. Svoboda, Channelrhodopsin-2-assisted circuit mapping of long-range callosal projections. *Nat. Neurosci.* **10**, 663–668 (2007).
24. K. T. Beier et al., Rabies screen reveals GPe control of cocaine-triggered plasticity. *Nature* **549**, 345–350 (2017).
25. N. Renier et al., Mapping of brain activity by automated volume analysis of immediate early genes. *Cell* **165**, 1789–1802 (2016).
26. T.-W. Chen, N. Li, K. Daie, K. Svoboda, A map of anticipatory activity in mouse motor cortex. *Neuron* **94**, 866–879.e4 (2017).
27. D. Lin et al., Functional identification of an aggression locus in the mouse hypothalamus. *Nature* **470**, 221–226 (2011).
28. L. A. DeNardo et al., Temporal evolution of cortical ensembles promoting remote memory retrieval. *Nat. Neurosci.* **22**, 460–469 (2019).
29. L. Ye et al., Wiring and molecular features of prefrontal ensembles representing distinct experiences. *Cell* **165**, 1776–1788 (2016).
30. B. N. Armbruster, X. Li, M. H. Pausch, S. Herlitze, B. L. Roth, Evolving the lock to fit the key to create a family of G protein-coupled receptors potently activated by an inert ligand. *Proc. Natl. Acad. Sci. U.S.A.* **104**, 5163–5168 (2007).
31. D. J. Urban, B. L. Roth, DREADDs (designer receptors exclusively activated by designer drugs): Chemogenetic tools with therapeutic utility. *Annu. Rev. Pharmacol. Toxicol.* **55**, 399–417 (2015).
32. T. J. Stachniak, A. Ghosh, S. M. Sternson, Chemogenetic synaptic silencing of neural circuits localizes a hypothalamus→midbrain pathway for feeding behavior. *Neuron* **82**, 797–808 (2014).
33. H. Arakawa, D. C. Blanchard, K. Arakawa, C. Dunlap, R. J. Blanchard, Scent marking behavior as an odorant communication in mice. *Neurosci. Biobehav. Rev.* **32**, 1236–1248 (2008).
34. J. L. Hurst, Urine marking in populations of wild house mice Mus domesticus rutty. I. Communication between males. *Anim. Behav.* **40**, 209–222 (1990).
35. A. W. Kaur et al., Murine pheromone proteins constitute a context-dependent combinatorial code governing multiple social behaviors. *Cell* **157**, 676–688 (2014).
36. M. V. Wu et al., Estrogen masculinizes neural pathways and sex-specific behaviors. *Cell* **139**, 61–72 (2009).
37. C. M. Williamson, I. S. Klein, W. Lee, J. P. Curley, Immediate early gene activation throughout the brain is associated with dynamic changes in social context. *Soc. Neurosci.*, 1–13 (2018).
38. S. A. Golden et al., Basal forebrain projections to the lateral habenula modulate aggression reward. *Nature* **534**, 688–692 (2016).
39. C. M. Williamson, R. D. Romeo, J. P. Curley, Dynamic changes in social dominance and mPOA GnRH expression in male mice following social opportunity. *Horm. Behav.* **87**, 80–88 (2017).
40. C. M. Williamson, W. Lee, R. D. Romeo, J. P. Curley, Social context-dependent relationships between mouse dominance rank and plasma hormone levels. *Physiol. Behav.* **171**, 110–119 (2017).
41. W. Lee, A. Khan, J. P. Curley, Major urinary protein levels are associated with social status and context in mouse social hierarchies. *Proc. Biol. Sci.* **284**, 20171570 (2017).
42. C. M. Williamson et al., Social hierarchy position in female mice is associated with plasma corticosterone levels and hypothalamic gene expression. *Sci. Rep.* **9**, 7324 (2019).
43. J. Kohl et al., Functional circuit architecture underlying parental behaviour. *Nature* **556**, 326–331 (2018).
44. W. E. Allen et al., Global representations of goal-directed behavior in distinct cell types of mouse neocortex. *Neuron* **94**, 891–907.e6 (2017).
45. N. Steinmetz, P. Zatka-Haas, M. Carandini, K. Harris, Distributed correlates of visually-guided behavior across the mouse brain. *Biorxiv*, 474437 (2018).
46. C. Stringer et al., Spontaneous behaviors drive multidimensional, brain-wide population activity. *Biorxiv*, 306019 (2018).
47. W. E. Allen et al., *Thirst Regulates Motivated Behavior through Modulation of Brainwide Neural Population Dynamics* (Sci New York, 2019).
48. J. J. Jun et al., Fully integrated silicon probes for high-density recording of neural activity. *Nature* **551**, 232–236 (2017).
49. N. J. Sofroniew, D. Flickinger, J. King, K. Svoboda, A large field of view two-photon mesoscope with subcellular resolution for in vivo imaging. *eLife* **5**, e14472 (2016).
50. J. Yao et al., Simultaneous measurement of neuronal activity in the pontine micturition center and cystometry in freely moving mice. *Front. Neurosci.* **13**, 663 (2019).
51. C. J. Fowler, D. Griffiths, W. C. de Groat, The neural control of micturition. *Nat. Rev. Neurosci.* **9**, 453–466 (2008).
52. L. Madisen et al., A robust and high-throughput Cre reporting and characterization system for the whole mouse brain. *Nat. Neurosci.* **13**, 133–140 (2010).
53. H. Taniguchi et al., A resource of Cre driver lines for genetic targeting of GABAergic neurons in cerebral cortex. *Neuron* **71**, 995–1013 (2011).
54. National Research Council, *Guide for the Care and Use of Laboratory Animals* (National Academies Press, Washington, DC, 8th Ed., 2011).
55. I. R. Wickersham, H. A. Sullivan, H. S. Seung, Production of glycoprotein-deleted rabies viruses for monosynaptic tracing and high-level gene expression in neurons. *Nat. Protoc.* **5**, 595–606 (2010).
56. S. C. Turaga et al., Convolutional networks can learn to generate affinity graphs for image segmentation. *Neural Comput.* **22**, 511–538 (2010).
57. S. Klein, M. Staring, K. Murphy, M. A. Viergever, J. P. Pluim, elastix: A toolbox for intensity-based medical image registration. *IEEE Trans. Med. Imaging* **29**, 196–205 (2010).
58. Y. Kim et al., Mapping social behavior-induced brain activation at cellular resolution in the mouse. *Cell Rep.* **10**, 292–305 (2015).
59. S. M. Sunkin et al., Allen brain atlas: An integrated spatio-temporal portal for exploring the central nervous system. *Nucleic Acids Res.* **41**, D996–D1008 (2013).
60. A. Saunders, A. J. Granger, B. L. Sabatini, Corelease of acetylcholine and GABA from cholinergic forebrain neurons. *eLife* **4**, e06412 (2015).
61. M. L. Wallace et al., Genetically distinct parallel pathways in the entopeduncular nucleus for limbic and sensorimotor output of the basal ganglia. *Neuron* **94**, 138–152.e5 (2017).
62. Y. Kim et al., Whole-brain mapping of neuronal activity in the learned helplessness model of depression. *Front. Neural Circuits* **10**, 3 (2016).
63. R. B. O'Hara, D. J. Kotze, Do not log-transform count data. *Methods Ecol. Evol.* **1**, 118–122 (2010).
64. W. N. Venables, B. D. Ripley, "The S language" in *Modern Applied Statistics with S* (Statistics and Computing, Springer, 2002), pp. 41–68.

NEUROSCIENCE

Hyun et al.
Social isolation uncovers a circuit underlying context-dependent territory-covering micturition

PNAS | 11 of 11
https://doi.org/10.1073/pnas.2018078118